

OH defects in quartz in granitic systems doped with spodumene, tourmaline and/or apatite: experimental investigations at 5–20 kbar

C. Frigo¹ · R. Stalder¹ · C. A. Hauzenberger²

Received: 6 April 2016 / Accepted: 2 July 2016 / Published online: 29 July 2016
© The Author(s) 2016. This article is published with open access at Springerlink.com

Abstract The incorporation of OH defects in quartz as a function of Li content in the bulk system and pressures was investigated. Quartz crystals were grown in water-saturated granitic systems, containing various amounts Li, B and P, supplied as accessory phases such as spodumene, tourmaline or apatite in the starting mixtures. High pressure experiments were performed at temperatures between 900 and 1100 °C, and pressures between 5 and 20 kbar with a piston cylinder apparatus, and the synthesized quartz crystals were analyzed by IR spectroscopy, electron microprobe and LA-ICP-MS spectroscopy. All IR absorption spectra revealed absorption features that can be assigned to AlOH (3313, 3379 and 3431 cm^{-1}) and $(4\text{H})_{\text{Si}}$ defects (3585 cm^{-1}), whereas quartz grown in the Li and B systems exhibited two additional bands related, respectively, to LiOH (3483 cm^{-1}) and BOH defects (3596 cm^{-1}). It was further observed that LiOH incorporation increases with higher spodumene content in the starting material and decreases with pressure, until no LiOH defects are observed at pressure higher than 15 kbar. Specifically, the most pronounced reduction of LiOH defects occurs in a rather narrow pressure interval (10–15 kbar) close to the high-quartz/low-quartz transition. However, the link between the transition and the defect incorporation remains unclear. Li total concentrations always exceed the Li-coupled LiOH defects, suggesting the simultaneous presence of dry AlLi defects. Results of this study suggest that LiOH defects are

detectable only in quartz crystals grown from middle and upper crustal sections (such as hydrothermal quartz) and not in quartz from deep roots of orogenic granitoids.

Keywords Quartz · OH defects · IR spectroscopy · Granite · Spodumene

Introduction

Quartz is one of the most abundant minerals on the Earth's crust. None of the less quartz is a phase that occurs in a broad variety of rocks and therefore crystallizes and equilibrates at different petrogenetic conditions. Quartz may contain different amounts of impurities such as H, Li, B, Na, Al, P, K, Ti, Fe, and Ge depending on the formation conditions at different geological environments (e.g., different temperatures, pressures and chemical environments). Some of these trace elements (i.e., Al and Ti) have been successfully applied as geothermometers (Dennen et al. 1970; Wark and Watson 2006; Thomas et al. 2010; Huang and Audétat 2012).

Methodologically, it is possible to determine the quartz grains provenience (1) by means of their luminescence caused by trace metal defects in cathodoluminescence (CL) spectroscopy (Zinkernagel 1978; Matter and Ramseyer 1985; Richter et al. 2003); (2) by chemical analysis of their trace content of impurity metals applied with the electron microprobe or LA-ICP-MS (Müller et al. 2003; Müller and Koch-Müller 2009), or (3) by their inventory of hydrous defects that charge compensate metal impurities involving mono-, tri- or pentavalent cations. In this respect, many studies focused on the determination of species and concentration of hydrous defects in quartz by Fourier transform infrared (FTIR) spectroscopic analyses.

✉ C. Frigo
corinne.frigo@uibk.ac.at

¹ Institut für Mineralogie und Petrographie, Universität Innsbruck, Innrain 52, 6020 Innsbruck, Austria

² Institut für Erdwissenschaften, Universität Graz, Universitätsplatz 2, 8010 Graz, Austria

Trace elements and hydrous defects are often incorporated in quartz by coupled substitutions of one silicon cation by trivalent (e.g., Al^{3+} , B^{3+} and Fe^{3+}) and monovalent (e.g., H^+ , Li^+ , K^+ and Na^+), or trivalent and pentavalent (e.g., P^{5+}) cations. Substitutions such as $\text{Si}^{4+} = \text{Al}^{3+} + \text{H}^+$ cause AIOH defects, which are characterized by three absorption bands at 3313, 3379 and 3431 cm^{-1} in the infrared range (Kats 1962; Bambauer 1963; Aines and Rossman 1984; Stalder and Konzett 2012). Other coupled substitutions involving the incorporation of protons in the quartz structure such as $\text{Si}^{4+} = \text{B}^{3+} + \text{H}^+$ and $\text{Si}^{4+} = 4\text{H}^+$ generate the BOH (Müller and Koch-Müller 2009) and the $(4\text{H})_{\text{Si}}$ hydrogarnet defect (Paterson 1986; Stalder and Konzett 2012), characterized by the bands at 3596 and 3585 cm^{-1} , respectively. The occurrence of the interstitial hydrous defects such as LiOH causes the absorption band at 3483 cm^{-1} (Kats 1962; Aines and Rossman 1984; Baron et al. 2015).

The intensity of these absorption bands depend on the prevailing conditions during crystallization or annealing and may be used to define the provenance of an individual quartz grain. For example, the hydrogarnet defect is a common point defect in synthetic quartz crystallized in a chemically pure system (Chakraborty and Lehmann 1976; Paterson 1986; Rovetta 1989). Concentrations of hydrogarnet in quartz from granitic systems are correlated to pressure (Stalder and Konzett 2012) and therefore may be used to distinguish between low- and high-pressure origins, while the concentration of AIOH defects is both temperature and pressure dependent, and cannot give additional information about the genesis conditions. In contrast, the concentration of BOH defects is not pressure dependent (Baron et al. 2015). Generally, quartz crystals of magmatic origin are mainly characterized by AIOH defects and therefore by higher incorporation of H^+ with respect to other rocks (Müller and Koch-Müller 2009; Stalder and Neuser 2013). In addition, rocks of pegmatitic origins are enriched in LiOH and BOH defects (Stalder and Neuser 2013). The major purpose of this work is a more detailed study to assess LiOH defects in the quartz structure depending on pressure and chemical system, with the aim to use this feature as petrological indicator. To achieve this goal, several high-pressure experiments were performed on a granite–spodumene system at pressures ranging from 5 to 20 kbar, which represents the pressure conditions from upper to lower crust in collision zones. Furthermore, few additional experiments on granite containing tourmaline and/or apatite were performed, in order to evaluate whether the charge neutrality equation $\text{H}^+ + \text{A}^+ + \text{P}^{5+} = \text{M}^{3+} + \text{B}^{3+}$, where A = alkali and M = metal ions (Müller and Koch-Müller 2009; Baron et al. 2015), is achieved.

Experimental and analytical methods

Starting materials

Quartz crystals were grown in the following systems: (1) quartz–granite–spodumene–water, (2) quartz–granite–tourmaline–water, (3) quartz–granite–apatite–water, (4) quartz–granite–spodumene–apatite–water and (5) quartz–granite–tourmaline–apatite–water. All starting materials consisted of synthetic quartz (Alfa Aesar 99.995 % purity) and natural granite from Sardinia/Italy, which was derived from the institute rock collection (68.90 wt% SiO_2 , 14.87 wt% Al_2O_3 , 6.35 wt% K_2O , 3.05 wt% Na_2O , 2.51 wt% Fe_2O_3 , 1.56 wt% CaO , 0.50 wt% MgO , 0.27 wt% TiO_2 , 0.08 wt% MnO , 0.04 wt% P_2O_5). Both synthetic quartz and natural granite powders were mixed in proportion of 1:1, partially molten in a platinum crucible at $1100\text{ }^\circ\text{C}$ for four hours, in order to promote the homogenization of the granitic components, and rapidly quenched to glass. The resulting glass + quartz mixture was successively ground to powder and finally mixed with different amounts of powdered spodumene, tourmaline and/or apatite, for doping the system with Li, B, and P, respectively. Details concerning the starting material are reported in Table 1.

High pressure experiments

Each solid mixture was filled together with 12–25 wt% water in Pt capsules with an outer (inner) diameter of 4.0 (3.6) mm. The capsule was then closed, welded shut, weighted and checked for leakage in an oven at $120\text{ }^\circ\text{C}$. The capsule was finally inserted in a BN sleeve, which produces an oxygen fugacity between CoCoO and WM (Truckenbrodt et al. 1997). All syntheses were performed in an end-loaded piston cylinder press using a NaCl assembly with graphite furnace. For experiments with pressures from 5 to 7.5 kbar a 22-mm assembly in combination with Pyrex sleeve was used, while a half-inch NaCl assembly was used for experiments at pressures from 10 to 20 kbar. Temperatures were monitored by using Ni–CrNi thermocouples. In order to promote crystal growth, the temperature was initially raised to 1100–1000 $^\circ\text{C}$ (Table 1), followed by a ramp down $900\text{ }^\circ\text{C}$ at a cooling rate of $20\text{ }^\circ\text{C/h}$. Temperatures were hold for 50–120 h (Table 1), and runs were terminated by shutting off the power supply.

The recovered capsules were then weighted, pierced, dried and weighted again, for verifying any fluid loss and quantifying the amount of water retained in the run products. If the products were fluid-saturated, it was possible to measure the fluid's pH, by pH indication paper, after piercing the capsule. The pH of the excess fluid was neutral or very weak alkalic (pH 6–7) for all the runs. Most

Table 1 Experimental conditions and starting material

Run #	Assembly (mm)	Capsule (mm)	Granite (mg)	Qz (mg)	Spd (mg)	Tur (mg)	Ap (mg)	Water (mg)	<i>P</i> (kbar)	<i>T</i> (°C)	<i>t</i> (h)
E16	NaCl-Pyrex 22	Pt 3.0	15.30	15.30	0.61	0.00	0.00	5.50	5	900	50
E33	NaCl-Pyrex 22	Pt 4.0	14.45	14.46	0.59	0.00	0.00	1.40	5	900	62
E24	NaCl-Pyrex 22	Pt 4.0	24.95	24.95	1.10	0.00	0.00	15.40	7.5	1050–900	96
E27	NaCl-Pyrex 22	Pt 4.0	24.75	24.74	1.01	0.00	0.00	9.80	7.5	1100–900	98
E17	NaCl 12.7	Pt 4.0	24.66	24.65	1.09	0.00	0.00	8.00	10	1000–900	96
E20	NaCl 12.7	Pt 4.0	27.05	27.05	0.00	0.00	0.00	15.20	10	1000–900	119
E21	NaCl 12.7	Pt 4.0	23.80	23.80	5.60	0.00	0.00	17.00	10	1000–900	53
E22	NaCl 12.7	Pt 4.0	23.75	23.75	0.00	0.00	2.50	15.30	10	1000–900	53
E23	NaCl 12.7	Pt 4.0	24.13	24.13	0.00	2.54	0.00	15.40	10	1000–900	77
E26	NaCl 12.7	Pt 4.0	20.04	20.03	9.93	0.00	0.00	17.00	10	1000–900	69
E29	NaCl 12.7	Pt 4.0	23.04	23.04	0.00	2.46	1.07	16.20	10	1000–900	71
E30	NaCl 12.7	Pt 4.0	24.68	24.68	5.74	0.00	2.93	18.60	10	1000–900	95
E19	NaCl 12.7	Pt 4.0	26.47	26.46	1.17	0.00	0.00	14.90	12.5	1030–900	72
E18	NaCl 12.7	Pt 4.0	25.19	25.19	1.11	0.00	0.00	18.00	15	1050–900	68
E14	NaCl 12.7	Pt 4.0	24.85	24.85	0.99	0.00	0.00	16.66	20	1050–900	95

Qz quartz, Spd spodumene, Tur tourmaline, Ap apatite

of the run products consisted exclusively of quartz crystals and quench material. In some runs, also spodumene (run: E30) and apatite crystals (runs: E29 and E30) could be observed (Fig. 1c), but may have also been present in very small proportions in other runs. It was also observed that quartz's crystal size changes in function of pressures and bulk composition of the starting material. Quartz crystals were then individually handpicked, mounted in thermoplastic resin and oriented parallel to the *c* axis with a polarizing microscope. Birefringence values of $\Delta n = 0.009$ in the orthoscopic view and “flash figures” in the conoscopic view confirmed a successful orientation of the quartz crystal. A λ -plate compensator was employed to determine the direction of the ordinary (n_o) and extraordinary (n_e) refractive indices, an essential prerequisite to perform polarized measurements with FTIR spectroscopy. Oriented crystals were manually ground, polished on both sides and finally removed from the resin by dissolution in acetone. Crystal thicknesses were measured with a mechanical Mitutoyo micrometer with an accuracy of $\pm 2 \mu\text{m}$. Characteristics of the prepared crystals including water concentrations are reported in Table 2.

FTIR spectroscopy

Mid-infrared spectra were recorded at room temperature in transmission mode by using a Bruker Vertex 70 FTIR spectrometer coupled to a Hyperion 3000 microscope, a nitrogen-cooled MCTD316-025 (mercury cadmium telluride) detector, a globar light source, a KBr beamsplitter and a wire grid polarizer. Background and

sample measurements were taken by averaging 32–300 scans, depending on the measured area that varied from 100×100 to $40 \times 40 \mu\text{m}^2$. Polarized measurements were taken along the ordinary (n_o) and extraordinary (n_e) refractive indexes on the same spot by turning the polarizers' direction by 90° . All IR bands related to OH defects are strongly polarized in the direction parallel to n_o and exhibit almost no absorbance in the direction parallel to n_e . Fluid/melt inclusions exhibit weak and broad absorption features in the OH range. Because of their isotropic behavior, the contribution of molecular water trapped as fluid micro-inclusions or in quench hydrous melt inclusions was eliminated by subtracting the n_e component from the n_o component of the OH absorption pattern according to the procedure described by Stalder and Konzett (2012). An additional correction described from Baron et al. (2015) was required for spectra containing BOH absorption bands, since the B-related OH defects exhibit a significant component for $E||n_e$. Water concentrations were calculated by integrating the polarized background-corrected IR spectra (normalized to thickness) across the region of absorption due to OH dipole vibrations ($3700\text{--}3200 \text{ cm}^{-1}$). The integrated extinction coefficients from mineral-specific (Aines et al. 1984; Thomas et al. 2009) and general wavelength-specific (Libowitzky and Rossman 1997) calibrations were used. All three calibrations yield for most samples results in excellent agreement to each other. Significant deviations only occur for spectra with strong absorptions in the high wavenumber range (Stalder and Konzett 2012; Baron et al. 2015), which are not relevant for the present study.

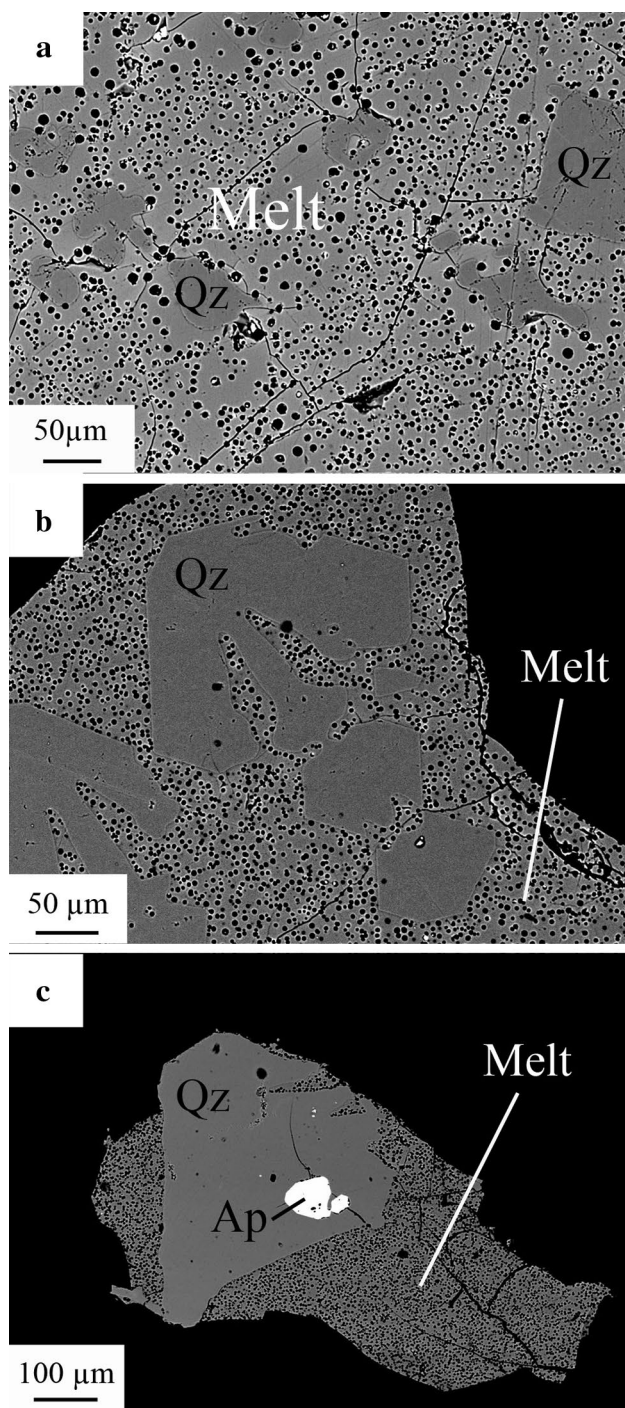


Fig. 1 BSE image of quartz (Qz) crystals in water-saturated melt from run E17 (a) and E20 (b) and euhedral apatite (Ap) crystals from runs E29 (c)

Electron microprobe

Textures from run products were inspected under a JEOL JXA-8100 electron microprobe (Fig. 1), and major and minor element chemistry of quartz crystals and quenched

melt were determined using 15 kV acceleration voltage. Concerning the beam current different analytical conditions were used depending on the measured material, 50 nA beam current on quartz for acquisition of the Al-K α line using a raster size of $12 \times 9 \mu\text{m}$, and 5 nA beam on quenched melt using a $6 \times 8 \mu\text{m}$ raster size. As standards, the following minerals were used: Si: quartz, Al: corundum, K: orthoclase, Na: jadeite, P: apatite, Fe: almandine, Mg: MgO, Ca: diopside, Ti: rutile, Mn: tephroite.

LA-ICP-MS

Trace element concentrations in quartz grains were analyzed by LA-ICP-MS (laser ablation unit: ESI NWR 193; ICP-MS: Agilent 7500ce) at the Central Lab for Water, Minerals and Rocks, NAWI Graz, Karl-Franzens-University of Graz and Graz University of Technology). The material was ablated by using a 193 nm laser pulsed at 10 Hz, 50 μm spot size with energy of $\sim 7.5 \text{ J cm}^{-2}$ and 11 Hz for measurements of 35 μm spot size, with energy of $\sim 8.5 \text{ J cm}^{-2}$. Helium was used as carrier gas at $\sim 0.6 \text{ l/min}$ flow, and data were acquired in time-resolved mode. For each analysis a 30 s gas blank was obtained for background correction, followed by 60 s of active laser and a wash out time of 45 s. NIST612 glass was used for standardization and drift correction, while NIST614 and SL-1 (G-Probe proficiency program, www.geoanalyst.org) were analyzed as unknowns to monitor the accuracy of the measurements. Both standards could be reproduced within $\pm 10 \%$ of the recommended values. Data reduction for quartz crystal analyses was performed using the software Glitter with silicon as internal standard, while element concentrations in the quench material was determined successively using the software SILLS (Guillong et al. 2008), which was gently granted from Dr. Markus Wälle from ETH, Zürich. For NIST612, the concentration values reported by Jochum et al. (2011) were used.

Results

IR band assignment and determination of water content as OH defects

All the IR absorption spectra revealed at least two specific absorption features, in particular a dominating triplet at 3313, 3379 and 3431 cm^{-1} , and a much weaker band at 3585 cm^{-1} , which can be assigned to AlOH defects (Kats 1961, 1962; Bambauer 1963) and hydrogarnet (4H)_{Si} defects, respectively. In addition, quartz crystals from the spodumene-bearing system show another band at 3483 cm^{-1} at pressures $\leq 10 \text{ kbar}$. This band corresponds to the LiOH defects and its absorbance is negatively correlated to pressure (Fig. 2). Quartz crystals grown in the

Table 2 IR measurements

Sample #	<i>P</i> (kbar)	Thickness (μm)	Water concentration (ppm)			Water as Li–OH (ppm)	
			T (09)	L&R (97)	A (84)	T (09)	L&R (97)
E16qz1	5	102	61.2	62.9	63.2	7.8	10.4
E24qz1	7.5	83	72.1	74.5	74.4	6.4	8.5
E24qz2	7.5	106	66.7	69.7	68.8	3.0	4.0
E24qz3	7.5	123	79.0	81.1	81.5	3.6	4.8
E24qz4	7.5	137	45.4	48.5	46.9	3.6	4.8
E24qz5	7.5	150	84.2	86.0	86.8	3.8	5.1
E27qz1	7.5	153	61.6	64.6	63.6	3.2	4.2
E27qz2	7.5	150	54.7	57.0	56.4	2.5	3.3
E27qz3	7.5	102	73.4	79.9	75.6	4.1	5.5
E27qz4	7.5	97	83.1	81.9	85.7	5.0	6.7
E27qz6	7.5	57	49.2	52.4	50.8	1.8	2.4
E17qz1	10	69	51.4	52.2	53.2	1.4	1.9
E17qz3	10	90	40.6	43.5	41.9	0.8	1.1
E17qz4	10	92	38.1	40.4	39.4	1.3	1.7
E17qz5	10	92	55.4	58.0	57.2	2.5	3.3
E17qz6	10	96	40.0	41.6	41.3	1.6	2.1
E17qz7	10	107	63.0	65.0	65.0	2.0	2.7
E20qz1	10	100	47.5	48.6	49.0	0.0	0.0
E20qz2_1	10	144	32.3	34.5	33.4	0.0	0.0
E20qz2_2	10	144	36.8	34.3	37.9	0.0	0.0
E20qz2_3	10	144	44.6	46.4	46.0	0.0	0.0
E20qz3	10	80	39.2	41.0	40.5	0.0	0.0
E21qz1	10	127	35.2	37.1	36.4	3.7	4.9
E21qz2	10	123	52.3	55.1	53.9	4.6	6.1
E21qz3	10	91	39.4	41.3	40.9	3.1	4.2
E22qz1	10	115	32.8	34.8	33.9	0.0	0.0
E22qz2	10	54	47.3	49.3	48.8	0.0	0.0
E22qz3	10	75	61.5	63.8	63.5	0.0	0.0
E22qz4	10	79	85.1	86.0	87.8	0.0	0.0
E22qz5	10	88	37.8	38.4	39.0	0.0	0.0
E23qz1	10	139	68.7	72.6	71.0	0.0	0.0
E23qz2	10	128	136.4	135.7	140.7	0.0	0.0
E23qz3	10	109	119.6	127.6	123.3	0.0	0.0
E23qz4	10	96	150.3	156.9	155.0	0.0	0.0
E23qz5	10	84	126.0	131.1	130.0	0.0	0.0
E23qz6	10	80	90.6	93.9	93.5	0.0	0.0
E23qz7	10	72	81.5	85.0	84.1	0.0	0.0
E26qz1	10	86	30.4	32.5	31.3	4.6	6.1
E26qz2	10	71	36.3	40.1	37.6	6.9	9.2
E29qz1	10	97	66.5	69.1	68.6	0.0	0.0
E29qz2	10	92	83.4	86.7	86.0	0.0	0.0
E30qz2	10	81	44.1	46.3	45.5	2.7	3.6
E30qz3	10	57	45.1	48.0	46.5	2.6	3.5
E19qz1	12.5	104	29.2	30.9	30.1	0.0	0.0
E19qz2	12.5	117	41.7	43.0	43.1	0.0	0.0
E19qz4	12.5	90	49.3	51.6	50.9	0.0	0.0
E19qz5	12.5	118	43.7	45.8	45.1	0.0	0.0

Table 2 continued

Sample #	P (kbar)	Thickness (μm)	Water concentration (ppm)			Water as Li–OH (ppm)	
			T (09)	L&R (97)	A (84)	T (09)	L&R (97)
E18qz1	15	98	42.4	44.6	43.7	0.0	0.0
E18qz3	15	97	29.6	31.9	30.5	0.0	0.0
E18qz4	15	74	39.9	43.0	41.1	0.0	0.0
E14qz1	20	155	34.6	36.8	35.7	0.0	0.0
E14qz2	20	105	41.4	44.0	42.7	0.0	0.0
E14qz3	20	104	43.9	47.0	45.3	0.0	0.0
E14qz4	20	145	27.2	28.8	28.5	0.0	0.0

T (09) = according to calibration of Thomas et al. (2009)

L&R (97) = according to calibration of Libowitzky and Rossman (1997)

A (84) = according to calibration of Aines et al. (1984)

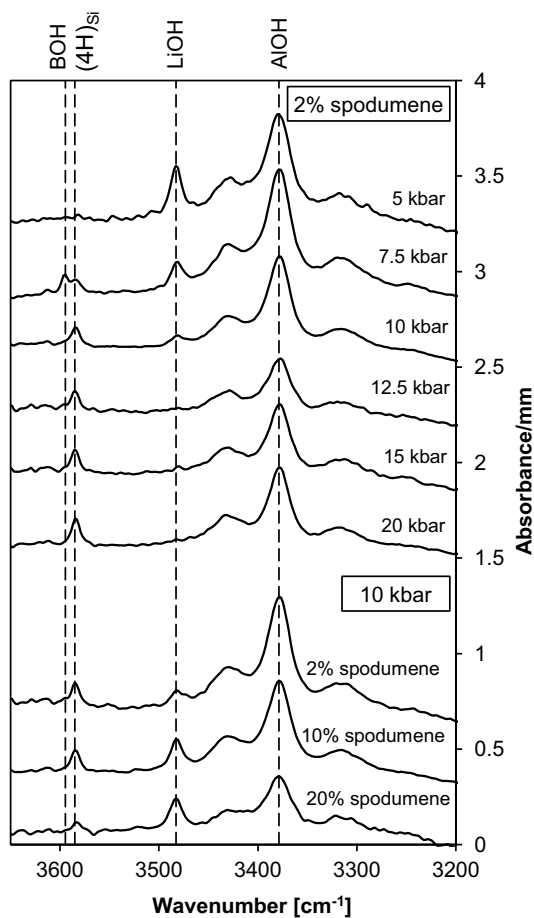


Fig. 2 IR spectra from quartz grown at different pressures (all with 2 % spodumene in the system) and different spodumene content in the system (all at 10 kbar)

tourmaline-bearing systems show an additional band at 3596 cm^{-1} that can be assigned to BOH defects (Müller and Koch-Müller 2009). The existence of a further band at 3469 cm^{-1} is not as clear. If this band is considered real, it

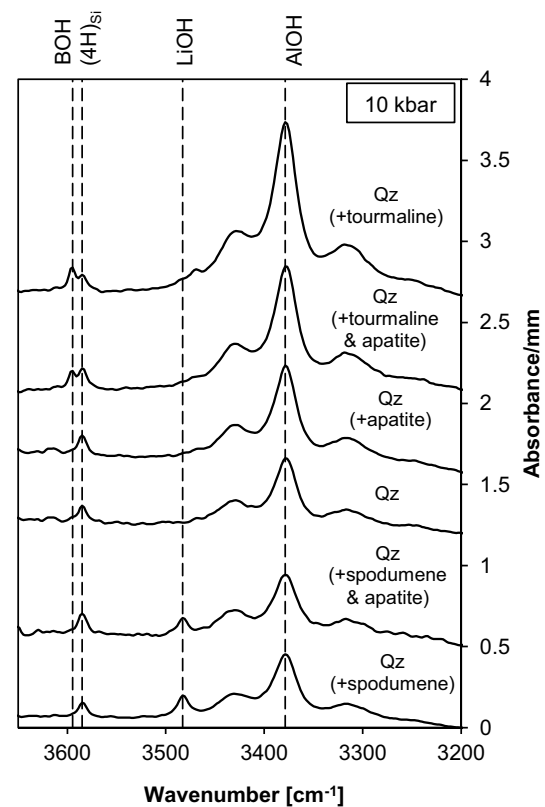


Fig. 3 IR spectra from quartz synthesized at 10 kbar in different bulk compositions containing different amounts of apatite, tourmaline and spodumene

may represent another Li-related defect (Kats 1961). Crystals grown in systems containing apatite did not show any additional bands; however, it is observed that the presence of apatite component in the bulk system show a weak negative effect on the intensities of OH bands related to trivalent cations, e.g., the B-related band at 3596 cm^{-1} and the Al-related band at 3379 cm^{-1} (Fig. 3).

Influence of chemical and physical parameters on OH incorporation

At 10 kbar, the LiOH concentration is correlated to the spodumene content in the starting material (Fig. 4). As this trend is followed up to high spodumene contents (i.e., 20 wt% in the bulk system), no evidence for saturation with respect to LiOH in quartz is apparent. At 5 kbar, very high LiOH concentrations in quartz are already observed at much lower spodumene contents (i.e., 2 wt%) in the system, suggesting that the saturation is reached at lower concentration levels and spodumene is less dissolved in the melt at lower pressure. Another experiment performed at 5 kbar with higher concentrations of spodumene in the bulk system would be critical to understand whether LiOH saturation already occurred. Such an experiment was performed (E33, Table 1). However, no crystals (neither spodumene nor quartz) could be observed in the run product neither under petrographic microscope, nor by XRD. Either the system was super-liquidus or nucleation was too sluggish to form crystals.

As far as the pressure effect on the OH incorporation in quartz is concerned, crystals grown from the starting material containing 2 % spodumene show not a clear trend, but a jump for the AlOH defects from ca. 60 wt ppm water at 5 kbar to a constant value of ca. 40 wt ppm water starting from 12.5 kbar (Fig. 5). This result slightly modifies previous experimental results on quartz in granitic systems, where a negative relation between AlOH concentrations and pressure was observed (Stalder and Konzett 2012; Baron et al. 2015).

Similar to AlOH, the LiOH content in quartz shows an evident negative correlation with pressures, and—at

2 wt% spodumene in the starting material—basically drops to zero at 12.5 kbar (Fig. 6). If we assume that similar trends occur at higher spodumene contents, LiOH defects could be present up to 15 kbar, but would

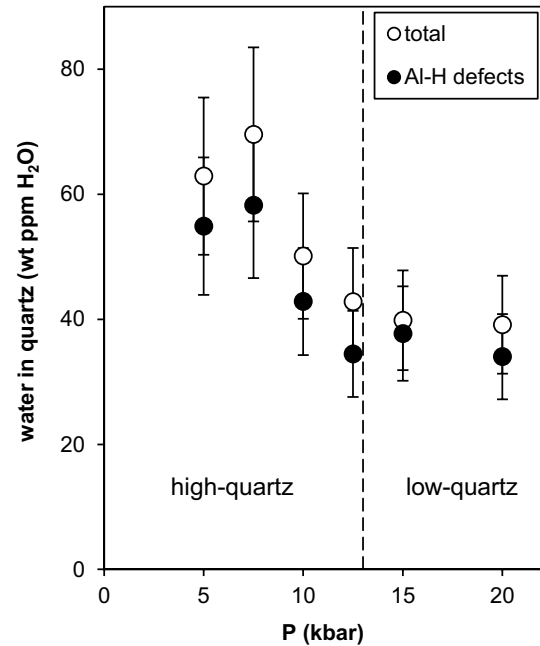


Fig. 5 Water concentrations as total amount of OH defects (*open circles*) and as Al-specific OH defects (*black circles*) from quartz grown in the 2 % spodumene system. The concentrations are expressed as wt ppm water using the calibration of Libowitzky and Rossman (1997). Error bars correspond to an absolute error of 20 %

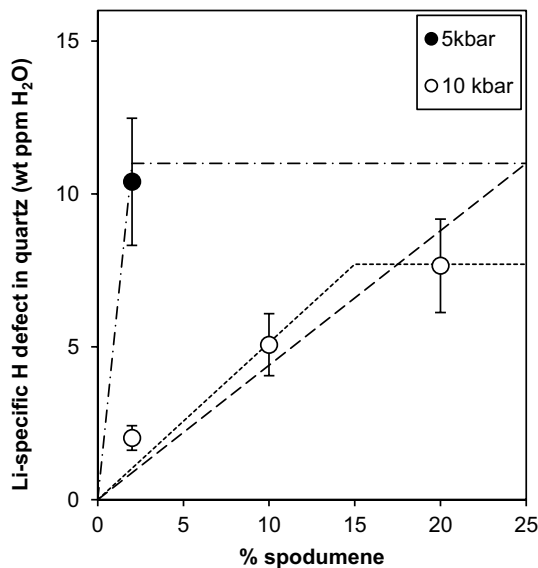


Fig. 4 OH content in quartz as LiOH defects against the spodumene content in the starting material (as wt ppm water)

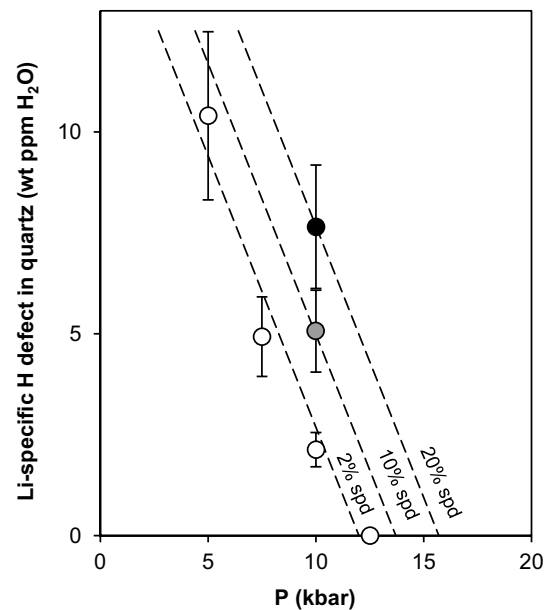


Fig. 6 Content of LiOH defects against pressure from quartz grown in the granitic system containing 2, 10 and 20 % spodumene

Table 3 Trace elements content in quartz and melt from electron microprobe analyses

Quartz											
No.	Na ₂ O (wt %)	Al ₂ O ₃ (wt %)	K ₂ O (wt %)	P ₂ O ₅ (wt %)	FeO (wt %)	SiO ₂ (wt %)	MgO (wt %)	TiO ₂ (wt %)	CaO (wt %)	MnO (wt %)	Tot
E16	b.d.l.	0.20 ± 0.07	b.d.l.	b.d.l.	b.d.l.	101.7 ± 0.6	n.a.	b.d.l.	n.a.	n.a.	101.9 ± 0.6
E33	n.m.	n.m.	n.m.	n.m.	n.m.	n.m.	n.m.	n.m.	n.m.	n.m.	n.m.
E24	b.d.l.	0.12 ± 0.02	b.d.l.	b.d.l.	b.d.l.	99.5 ± 0.5	b.d.l.	b.d.l.	b.d.l.	b.d.l.	101.9 ± 0.6
E27	b.d.l.	0.08 ± 0.01	b.d.l.	b.d.l.	b.d.l.	98.1 ± 1.0	n.a.	b.d.l.	n.a.	n.a.	98.3 ± 1.0
E17	b.d.l.	0.06 ± 0.02	b.d.l.	b.d.l.	b.d.l.	99.2 ± 0.7	n.a.	b.d.l.	n.a.	n.a.	99.3 ± 0.7
E19	b.d.l.	0.05 ± 0.01	b.d.l.	b.d.l.	b.d.l.	100.9 ± 0.6	n.a.	b.d.l.	n.a.	n.a.	100.9 ± 0.6
E18	b.d.l.	0.05 ± 0.00	b.d.l.	b.d.l.	b.d.l.	101.0 ± 0.5	n.a.	b.d.l.	n.a.	n.a.	101.0 ± 0.5
E14	b.d.l.	0.04 ± 0.01	b.d.l.	b.d.l.	b.d.l.	99.5 ± 0.4	n.a.	b.d.l.	n.a.	n.a.	99.5 ± 0.4
E21	b.d.l.	0.15 ± 0.04	b.d.l.	b.d.l.	b.d.l.	101.1 ± 0.4	n.a.	b.d.l.	n.a.	n.a.	101.3 ± 0.3
E26	n.a.	n.a.	n.a.	n.a.	n.a.	n.a.	n.a.	n.a.	n.a.	n.a.	n.a.
E20	b.d.l.	0.02 ± 0.00	b.d.l.	b.d.l.	b.d.l.	100.3 ± 0.4	n.a.	b.d.l.	n.a.	n.a.	100.4 ± 0.4
E22	b.d.l.	0.13 ± 0.03	b.d.l.	b.d.l.	b.d.l.	100.1 ± 0.1	b.d.l.	b.d.l.	b.d.l.	b.d.l.	100.4 ± 0.1
E23	b.d.l.	0.10 ± 0.01	b.d.l.	b.d.l.	b.d.l.	99.6 ± 0.1	b.d.l.	b.d.l.	b.d.l.	b.d.l.	99.7 ± 0.1
E29	b.d.l.	0.07 ± 0.01	b.d.l.	b.d.l.	b.d.l.	98.2 ± 0.6	n.a.	b.d.l.	n.a.	n.a.	98.3 ± 0.6
E30	b.d.l.	0.10 ± 0.05	b.d.l.	b.d.l.	b.d.l.	99.2 ± 0.6	n.a.	b.d.l.	n.a.	n.a.	99.3 ± 0.6
Melt											
No.	Na ₂ O (wt %)	Al ₂ O ₃ (wt %)	K ₂ O (wt %)	P ₂ O ₅ (wt %)	FeO (wt %)	SiO ₂ (wt %)	MgO (wt %)	TiO ₂ (wt %)	CaO (wt %)	MnO (wt %)	Tot
E16	b.d.l.	b.d.l.	b.d.l.	b.d.l.	b.d.l.	b.d.l.	b.d.l.	b.d.l.	b.d.l.	b.d.l.	b.d.l.
E33	n.m.	n.m.	n.m.	n.m.	n.m.	n.m.	n.m.	n.m.	n.m.	n.m.	n.m.
E24	1.3 ± 0.1	7.2 ± 0.2	2.8 ± 0.1	b.d.l.	b.d.l.	76.0 ± 0.5	0.27 ± 0.03	0.12 ± 0.03	0.63 ± 0.05	b.d.l.	88.3 ± 0.5
E27	1.3 ± 0.2	9.4 ± 0.1	3.7 ± 0.1	b.d.l.	b.d.l.	73.4 ± 0.3	n.m.	0.15 ± 0.02	n.m.	b.d.l.	88.0 ± 0.3
E17	1.4 ± 0.1	8.5 ± 0.2	3.2 ± 0.1	b.d.l.	b.d.l.	74.8 ± 0.5	0.32 ± 0.02	0.15 ± 0.03	0.81 ± 0.05	b.d.l.	89.2 ± 0.6
E19	1.3 ± 0.1	8.5 ± 0.2	3.0 ± 0.1	b.d.l.	b.d.l.	75.2 ± 0.7	0.32 ± 0.03	0.13 ± 0.02	0.85 ± 0.09	b.d.l.	89.4 ± 0.8
E18	n.m.	n.m.	n.m.	n.m.	n.m.	n.m.	n.m.	n.m.	n.m.	n.m.	n.m.
E14	1.4 ± 0.1	9.1 ± 0.3	3.5 ± 0.1	b.d.l.	b.d.l.	57.4 ± 4.0	n.m.	0.13 ± 0.03	n.m.	b.d.l.	71.5 ± 4.2
E21	1.3 ± 0.1	9.0 ± 0.3	2.8 ± 0.1	b.d.l.	b.d.l.	74.7 ± 0.6	0.25 ± 0.05	0.10 ± 0.03	0.57 ± 0.06	b.d.l.	88.6 ± 0.6
E26	1.0 ± 0.1	10.3 ± 0.3	2.4 ± 0.1	b.d.l.	b.d.l.	73.4 ± 1.8	n.m.	0.08 ± 0.04	n.m.	b.d.l.	87.2 ± 1.6
E20	1.4 ± 0.1	7.3 ± 0.4	3.1 ± 0.1	b.d.l.	b.d.l.	77.1 ± 0.5	0.29 ± 0.03	0.13 ± 0.04	0.79 ± 0.04	b.d.l.	90.2 ± 0.7
E22	1.8 ± 0.1	9.0 ± 0.2	3.5 ± 0.1	b.d.l.	b.d.l.	73.5 ± 1.3	0.34 ± 0.02	0.14 ± 0.04	0.97 ± 0.03	b.d.l.	89.3 ± 1.4
E23	1.7 ± 0.1	9.8 ± 0.3	3.4 ± 0.1	b.d.l.	b.d.l.	71.4 ± 0.4	0.42 ± 0.03	0.12 ± 0.03	0.67 ± 0.05	b.d.l.	87.6 ± 0.5
E29	1.3 ± 0.1	8.7 ± 0.1	3.0 ± 0.1	b.d.l.	b.d.l.	74.8 ± 0.7	n.m.	0.12 ± 0.02	n.m.	b.d.l.	88.2 ± 0.7
E30	1.3 ± 0.1	9.0 ± 0.3	2.7 ± 0.1	b.d.l.	b.d.l.	75.7 ± 1.1	n.m.	0.10 ± 0.03	n.m.	b.d.l.	88.7 ± 1.0

n.m. not measured, n.a. not analyzed, b.d.l. below the detection limit

disappear even in extremely Li-rich systems at even higher pressures.

Electron microprobe and LA-ICP-MS results

Quartz, melt and accessory phases such as apatite were observed in BSE images (Fig. 1). Comparison of

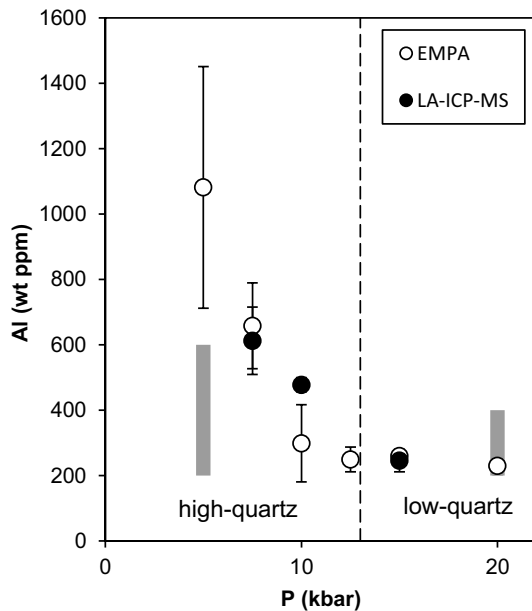


Fig. 7 Al contents in quartz against pressure from EMPA (*open circles*) and LA-ICP-MS (*black circles*) from runs containing 2 % spodumene. *Areas in gray* represent the results from Stalder and Konzett (2012)

quantitative analyses from electron microprobe and LA-ICP-MS was used as tool to discriminate between measurements of inclusion-free quartz and those containing melt inclusions (see Fig. 1a). The following two criteria were interpreted as sign for melt contamination: (1) an unreasonable high concentration of K (>100 ppm), as extremely incompatible element, and/or (2) a deviation in Al content measured by LA-ICP-MS by more than 3σ from the value determined by electron microprobe. Data points that showed such characteristics were considered as contaminated by tiny melt inclusions and were omitted from the data set. Data points from inclusion-free quartz and melt compositions from electron microprobe analyses are reported in Table 3. At constant temperature, Al in quartz shows a negative trend against pressure and decreases from 1000 ppm at 5 kbar to values around 250 ppm at 20 kbar (Fig. 7), in good agreement with the results of Stalder and Konzett (2012). The analytical totals from the measurements taken on melts are below 100 wt%, suggesting dissolution of water in the melt. Melts that formed between 7.5 and 12.5 kbar (i.e., below the second critical endpoint) typically show analytical totals of ~90 wt%, indicating ~10 wt% water content, whereas amorphous quench formed at 20 kbar show analytical totals of ~70 wt%, which corresponds to ~30 wt% water (Table 3).

LA-ICP-MS analytical results are reported in Table 4. Quartz crystals from some runs could not be analyzed, either because the grain size was too small to perform analyses on inclusion-free spots either due to the explosion of the sample caused by the overheating of fluid inclusions beneath the measured surface during laser irradiation.

Table 4 LA-ICP-MS measurements

	LA-ICP-MS quartz					LA-ICP-MS melt
	Li (wt ppm)	B (wt ppm)	Al (wt ppm)	P (wt ppm)	K (wt ppm)	Al/Li
E16	n.a.	n.a.	n.a.	n.a.	n.a.	n.a.
E33	n.a.	n.a.	n.a.	n.a.	n.a.	n.a.
E24	64 ± 7	4 ± 0.2	612 ± 103	16 ± 3	2 ± 0.8	65 ± 47
E27	n.a.	n.a.	n.a.	n.a.	n.a.	90
E17	49 ± 2	3 ± 0.2	478 ± 22	11 ± 3	<0.83 ± 0.3	35 ± 18
E20	n.a.	n.a.	n.a.	n.a.	n.a.	1334 ± 221
E21	194 ± 37	2 ± 1	1080 ± 291	10 ± 10	8 ± 2	16 ± 1
E22	2 ± 0.4	2 ± 0.1	196 ± 13	17 ± 3	<1.15 ± 0.1	n.a.
E23	3 ± 0.1	11 ± 0.3	557 ± 16	13 ± 4	<0.77 ± 0.0	621 ± 374
E26	337 ± 5	2 ± 0.1	1630 ± 33	12 ± 2	15 ± 0.0	6 ± 1
E29	2 ± 0.2	8 ± 1	425 ± 52	13 ± 1	<0.77 ± 0.0	n.a.
E30	81 ± 4	1 ± 0.2	451 ± 27	12 ± 3	<0.74 ± 0.3	9 ± 0.3
E19	n.a.	n.a.	n.a.	n.a.	n.a.	44 ± 8
E18	18 ± 2	2 ± 0.1	246 ± 34	15 ± 3	5 ± 8	32 ± 18
E14	n.a.	n.a.	n.a.	n.a.	n.a.	n.a.

n.a. not analyzed

LA-ICP-MS data points from the quench material exhibit a very high standard deviation, which in some cases was even higher than the mean value. However, the ratio Al/Li within one sample was nearly constant, and therefore, results from the quench material are reported as Al/Li ratio.

Discussion

Li saturation

Based on the observation of Li-specific (3483 cm^{-1}) and Al-specific (3379 cm^{-1}) OH bands, different OH environments exist. The linear correlation of Li-specific OH and spodumene content in the starting material observed at 10 kbar (Fig. 4) suggests that the system is not saturated with respect to Li even at highest Li content investigated at 10 kbar. If spodumene is added to undoped granite up to 10 wt% spodumene in the starting material, the resulting quartz increases its Li-specific OH without changing the Al-specific OH significantly (Fig. 8). Further input of spodumene leads to a further increase in Li-specific OH accompanied with a decrease of Al-specific OH. This leads to the conclusion that Li is incorporated in different local environments, one of which increasing the total OH (presumably as LiOH) and the other

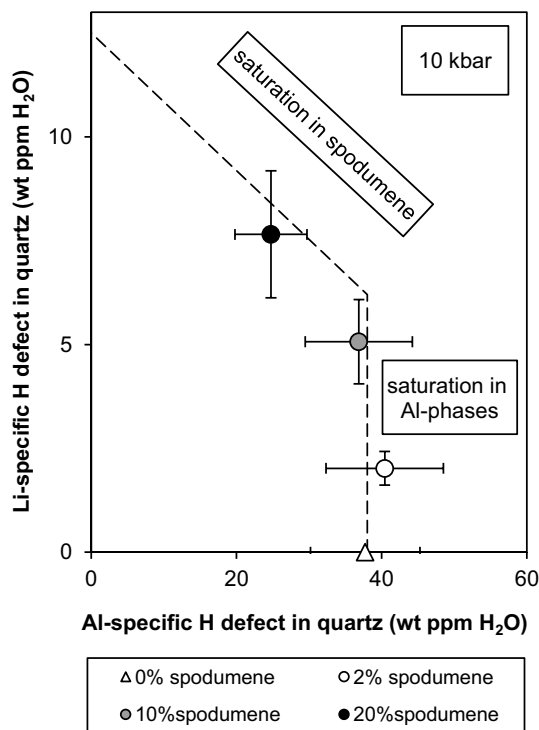


Fig. 8 Relation of LiOH defect and AlOH defect concentrations in quartz at 10 kbar. The kink in the trend suggests a change in the saturation regime (see text for discussion)

counteracting OH incorporation by combining with Al ($\text{Si}^{4+} = \text{Al}^{3+} + \text{Li}^+$) and reducing the coupling capacity of Al to protons ($\text{Si}^{4+} = \text{Al}^{3+} + \text{H}^+$). The kink in the LiOH–AlOH-plot may further suggest that saturation with respect to Li was reached (see dotted line in Fig. 4).

Charge balance involving H and other impurities

According to previous studies charge balance of impurities in quartz is achieved by $\text{H}^+ + \text{A}^+ + \text{P}^{5+} = \text{M}^{3+} + \text{B}^{3+}$, with A = alkali ions and M = metal ions (Müller and Koch-Müller 2009; Baron et al. 2015). In order to account for the contrasting role of Li, two different species for Li have to be defined: (I) Li_I decreasing the OH content by forming a dry AlLi defect, and (II) Li_{II} increasing the OH content by incorporation of LiOH and formation of non-bridging oxygens (Kats 1961). Li_{II} was calculated from the absorption band in the IR spectrum, and Li_I was calculated by subtracting Li_{II} from total Li determined by LA-ICP-MS. Data points show a linear correlation (Fig. 9), but deviate systematically by some 15 % toward the trivalent cations. The reason for this mismatch is unknown. A major contribution of incorrect Li assignment is excluded due to the rather low Li concentrations. A better explanation is the accuracy of the IR calibration for the quantification of water contents.

Pressure effect

IR spectra of OH defects in quartz show systematic variations with pressure and the Li-specific band at 3483 cm^{-1} is reduced with increasing pressure at a given

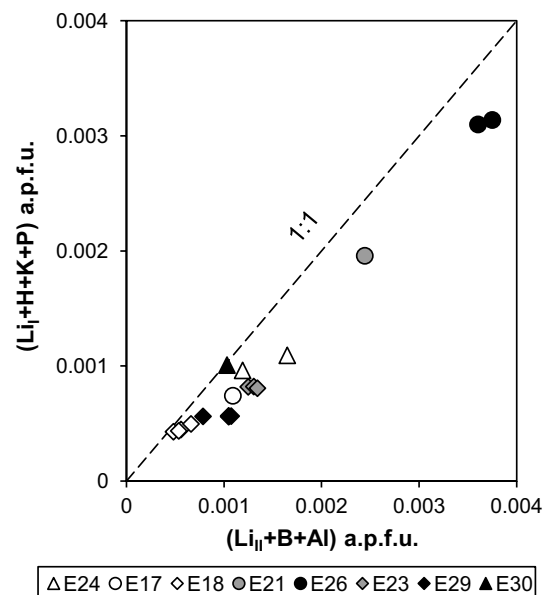


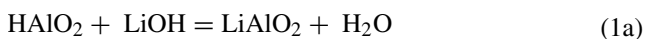
Fig. 9 Coupled substitutions of H^+ , Li^+ , K^+ , Al^{3+} , P^{5+} and B^{3+} . Li_I corresponds to AlLi defects and Li_{II} to LiOH defects

Table 5 Chemistry of quartz and melt, partition coefficients $D_{\text{Li}}^{\text{qtz/melt}}$, $D_{\text{Al}}^{\text{qtz/melt}}$ and $D_{\text{H}}^{\text{qtz/melt}}$, K and Al content in starting material and degree of melting

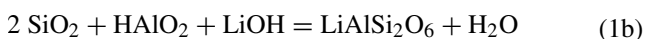
# Run	Quartz (wt ppm)			Melt (wt %)				Partition coefficient ^{qtz/melt}			Starting material		Degree of melting (%)		
	Li ^a	Al ^b	H ₂ O ^c	Li ₂ O ^d	K ₂ O ^b	Al ₂ O ₃ ^b	H ₂ O ^d	$D_{\text{Li}}^{\text{qtz/melt}}$	$D_{\text{Al}}^{\text{qtz/melt}}$	$D_{\text{H}}^{\text{qtz/melt}}$	K ₂ O	Al ₂ O ₃	K ₂ O	Al ₂ O ₃	Average
	(ppm)	(ppm)	(ppm)	(wt %)	(wt %)	(wt %)	(wt %)				(wt %)	(wt %)			
E16	–	–	–	–	–	–	–	–	–	–	–	–	–	–	–
E33	–	–	–	–	–	–	–	–	–	–	2	8	–	–	–
E24	64	659	72	0.2	3	7	12	0.089	0.017	0.0006	3	7	92	94	93
E27	–	396	67	–	4	9	12	–	0.008	0.0006	3	7	69	70	70
E17	49	299	50	0.2	3	8	11	0.058	0.007	0.0005	3	7	80	83	82
E19	–	250	43	–	3	8	11	–	0.006	0.0004	2	6	73	81	77
E18	18	260	40	–	–	–	–	–	–	–	2	6	–	–	–
E14	–	230	39	–	3	9	29	–	0.005	0.0001	2	6	65	67	66
E21	194	786	45	0.8	3	9	11	0.052	0.017	0.0004	2	7	81	78	79
E26	337	1630 ^a	36	1.5	2	10	13	0.050	0.030	0.0003	2	9	80	80	80
E20	–	122	41	–	3	7	10	–	0.003	0.0004	2	6	79	81	80
E22	2	691	54	0.0	4	9	11	–	0.015	0.0005	2	5	60	66	63
E23	3	538	115	0.0	3	10	12	–	0.010	0.0009	2	7	67	68	67
E29	2	361	78	0.0	3	9	12	–	0.008	0.0007	2	6	72	74	73
E30	81	542	47	0.8	3	9	11	0.022	0.011	0.0004	2	7	76	77	77

^a Concentrations determined LA-ICP-MS^b Concentrations determined electron microprobe^c Concentrations determined by IR spectroscopy^d Concentrations calculated

starting composition. If we consider endmember compositions for coupled substitutions such as HAIO_2 (for $\text{Si}^{4+} = \text{Al}^{3+} + \text{H}^+$) and LiAlO_2 (for $\text{Si}^{4+} = \text{Al}^{3+} + \text{Li}^+$), increasing pressure shifts the reaction



or



to the right and in this way reduces the total amount of OH defects. Based on the present results most of the shift in the reaction seems to occur at a rather narrow pressure interval, namely between 10 and 15 kbar. In this pressure interval falls the transition from high-quartz to low-quartz (Mirwald and Massonne 1980). If the high-/low-quartz transition were relevant for the preferred incorporation of LiAl defects, we would expect lower LiAl defects at high pressure, because $\text{LiAlSi}_2\text{O}_6$ can crystallize in high-quartz structure (London 1984), which is stable below 13 kbar. However, according to reaction (1a) and (1b), the LiAl component is better incorporated above 13 kbar, which makes a connection of this hypothesis and the high-/low-quartz transition questionable. On the other hand, as far as total concentrations of Li and Al are concerned, the

negative correlation to pressure (Fig. 7) seems to be in accord to the preferred LiAl coupling in the high-quartz field (i.e., at low pressure). The appearance of a dominant LiOH absorption band at 3483 cm^{-1} seems to be related to quartz that crystallized at rather low pressures. Samples from nature with these characteristics exist, such as large hydrothermal quartz crystals that grew in the roof region of late stage magmatic systems and show a high LiOH/AlOH band ratio, e.g., the rock crystal from Brazil reported in Stalder and Neuser (2013).

Partitioning of Al, Li and H between quartz and melt

Since concentrations of Li in the melt could not be measured directly, Li concentrations in the quenched melt were calculated by mass balance. In order to do this, in a first step melt fractions were calculated from K_2O and Al_2O_3 content in the melt (the only significant repository of these elements). Furthermore, it was assumed that only insignificant amounts of Li are dissolved in the excess fluid after the experiment, because the pH of the fluid phase was close to neutral. Consequently, also Li was considered to be hosted mainly in the melt, and its concentrations were calculated based on the melt fraction calculated before. Hydrogen

concentrations in the melts were calculated by subtracting the electron microprobe's analytical totals from 100 %. Concentrations were used to determine partition coefficients for Al, Li and H between quartz and melt, which follow the order $D_{\text{Li}}^{\text{qtz/melt}} > D_{\text{Al}}^{\text{qtz/melt}} > D_{\text{H}}^{\text{qtz/melt}}$ (Table 5). At 10 kbar, three different correlations are observed between the Log of $D_{\text{Li}}^{\text{qtz/melt}}$, $D_{\text{Al}}^{\text{qtz/melt}}$, $D_{\text{H}}^{\text{qtz/melt}}$ and the spodumene content in the starting material (Fig. 10), that is (1) an almost horizontal trend for Li, (2) a clear positive trend for Al and (3) a slightly negative trend for H. In particular, the trends for $D_{\text{Li}}^{\text{qtz/melt}}$ and $D_{\text{Al}}^{\text{qtz/melt}}$ converge at 20 wt% spodumene and a kink for $D_{\text{Al}}^{\text{qtz/melt}}$ between 10 and 15 wt% of spodumene content in the starting material is observed. The convergence and the kink might confirm the hypothesis that the system is saturated in spodumene for these conditions. Pressure does also affect the partitioning of Li, Al and H between quartz and melt. Experiments performed on starting material containing 2 wt% spodumene at pressures between 5 and 20 kbar, show in fact a negative correlation between the Log of $D_{\text{Li}}^{\text{qtz/melt}}$, $D_{\text{Al}}^{\text{qtz/melt}}$, $D_{\text{H}}^{\text{qtz/melt}}$ and pressure (Fig. 11). All the trends present the same inclination, suggesting that Li, Al and H incorporations are related.

The effect of apatite on defects incorporation in quartz

In this study it is observed that the presence of apatite in the bulk system has only a weak effect on the intensities of OH

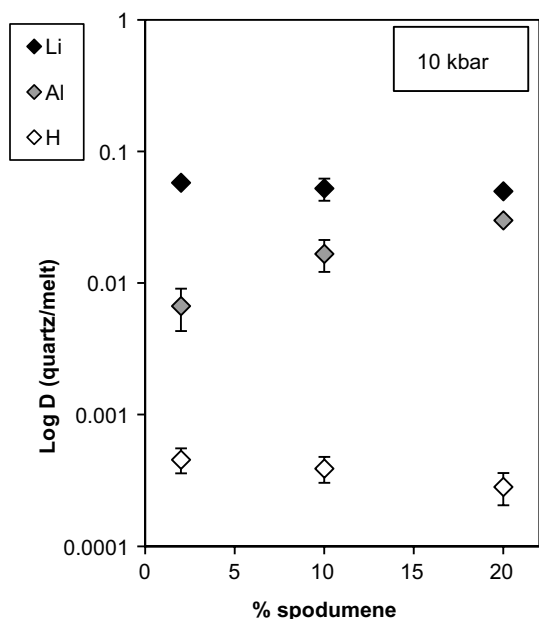


Fig. 10 Relations between the Log D(quartz/melt) of Li, Al, H and spodumene concentration in the starting material for experiments performed at 10 kbar. $D_{\text{Al}}^{\text{quartz/melt}}$ shows a positive trend that kinks between 10 and 20 wt% spodumene and converges with $D_{\text{Li}}^{\text{quartz/melt}}$ at 20 wt% spodumene. These particular features might confirm the hypothesis of a change in the saturation regime

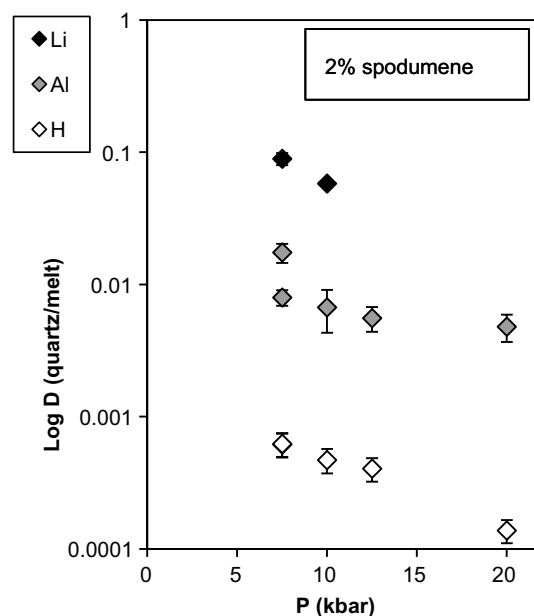


Fig. 11 Relations between the Log D(quartz/melt) of Li, Al, H and pressure for experiments performed with starting materials containing 2 wt% spodumene. All the trends show the same negative inclination

bands. LA-ICP-MS measurements revealed constant concentrations of 10–17 ppm P in quartz for all run products, suggesting that even the undoped system was saturated by apatite, even if it was only observed in BSE images at higher concentration levels (Fig. 1c). A weak coupling of P^{5+} to B^{3+} and Al^{3+} is possible, as apatite slightly reduces the AIOH and BOH bands in when added to the tourmaline-doped system (Fig. 3). High concentrations of P in the starting material may further influence phase and melting relation and therefore indirectly affect the trace elements incorporation (including OH defects) in quartz.

Compared to quartz from natural samples, phosphorous in quartz is well within the reported range for P_2O_5 enriched granites and monazite-bearing pegmatites that contain 7–10 ppm P (Breiter and Müller 2009) and 9–23 ppm P (Larsen et al. 2004), respectively.

Acknowledgments Open access funding were provided by University of Innsbruck and Medical University of Innsbruck. We like to thank Hannes Witting for manufacturing the high-pressure assemblies and Philipp Mair for helping in performing high-pressure experiments E16 and E33. Many thanks also to Richard Tessadri for XRF analysis on the starting material, Martina Tribus for the calibration of the electron microprobe and Daniela Schmidmair for XRD analysis.

Open Access This article is distributed under the terms of the Creative Commons Attribution 4.0 International License (<http://creativecommons.org/licenses/by/4.0/>), which permits unrestricted use, distribution, and reproduction in any medium, provided you give appropriate credit to the original author(s) and the source, provide a link to the Creative Commons license, and indicate if changes were made.

References

- Aines RD, Rossman GR (1984) Water in minerals? A peak in the infrared. *J Geophys Res* 89:4059–4071
- Aines RD, Kirby SH, Rossman GR (1984) Hydrogen speciation in synthetic quartz. *Phys Chem Miner* 11:204–212
- Bambauer HU (1963) Merkmale des OH-Spektrums alpiner Quarze (3 μ -Gebiet). *Schweiz Miner Petrog* 43:259–268
- Baron MA, Stalder R, Hauzenberger CA (2015) OH-point defects in quartz in B- and Li-bearing systems and their application to pegmatites. *Phys Chem Miner* 42:53–62
- Breiter K, Müller A (2009) Evolution of rare-metal granitic magmas documented by quartz chemistry. *Eur J Mineral* 21:335–346
- Chakraborty D, Lehmann G (1976) Distribution of OH in synthetic and natural quartz crystals. *J Solid State Chem* 17:305–311
- Dennen WH, Blackburn WH, Quesada A (1970) Aluminium in quartz as a geobarometer. *Contrib Mineral Petrol* 27:332–342
- Guillong M, Meier DL, Allan MM, Heinrich CA, Yardley BWD (2008) SILLS: a matlab-based program for the reduction of laser ablation ICP-MS data of homogeneous materials and inclusions. *Mineral Assoc Canada Short Course* 40:328–333
- Huang R, Audétat A (2012) The titanium-in-quartz (TitaniQ) thermometer: a critical examination and re-calibration. *Geochim Cosmochim Acta* 84:75–89
- Jochum KP, Weis U, Stoll B, Kuzmin D, Yang Q, Raczek I, Jacob DE, Stracke A, Birbaum K, Frick DA, Günther D, Enzweiler J (2011) Determination of reference values for NIST SRM 610–617 glasses following ISO guidelines. *Geostand Geoanal Res* 35:397–429
- Kats A (1961) Hydrogen in alpha quartz. Dissertation, Delft University of Technology, Netherland
- Kats A (1962) Hydrogen in alpha quartz. *Philips Res Rep* 17:133–279
- Larsen RB, Henderson I, Ihlen PM, Jacamon F (2004) Distribution and petrogenetic behavior of trace elements in granitic pegmatite quartz from South Norway. *Contrib Mineral Petrol* 147:615–628
- Libowitzky E, Rossman GR (1997) An IR calibration for water in minerals. *Am Mineral* 82:1111–1115
- London D (1984) Experimental phase equilibria in the system LiAl-SiO₄-SiO₂-H₂O: a petrogenetic grid for lithium-rich pegmatites. *Am Mineral* 69:995–1004
- Matter A, Ramseyer K (1985) Cathodoluminescence microscopy as a tool for provenance studies of sandstones. *NATO ASI Series* 148:191–211
- Mirwald PW, Massonne HJ (1980) The low-high quartz and quartz-coesite transition to 40 kbar between 600 °C and 1600 °C and some reconnaissance data on the effect of NaAlO₂ component on the low quartz-coesite transition. *J Geophys Res* 85:6983–6990
- Müller A, Koch-Müller M (2009) Hydrogen speciation and trace element contents of igneous, hydrothermal and metamorphic quartz from Norway. *Mineral Mag* 73:569–583
- Müller A, Wiedenbeck M, Van den Kerkhof AM, Kronz A, Simon K (2003) Trace elements in quartz: a combined electron microprobe, secondary ion mass spectrometry, laser-ablation ICP-MS and cathodoluminescence study. *Eur J Mineral* 15:747–763
- Paterson MS (1986) The thermodynamics of water in quartz. *Phys Chem Miner* 13:245–255
- Richter DK, Götze T, Götze J, Neuser RD (2003) Progress and application of cathodoluminescence (CL) in sedimentary petrology. *Miner Petrol* 79:127–166
- Rovetta MR (1989) Experimental and spectroscopic constraints on the solubility of hydroxyl in quartz. *Phys Earth Planet Int* 55:326–334
- Stalder R, Konzett J (2012) OH-defects in quartz in the system quartz-albite-water and granite water between 5 and 25 kbar. *Phys Chem Miner* 39:817–827
- Stalder R, Neuser RD (2013) OH-defects in detrital quartz grains: potential for application as tool for provenance analysis and overview over crustal average. *Sediment Geol* 294:118–126
- Thomas SM, Koch-Müller M, Reichart P, Rhede D, Thomas R, Wirth R (2009) IR calibrations for water determination in olivine, r-GeO₂ and SiO₂ polymorphs. *Phys Chem Miner* 36:489–509
- Thomas JB, Watson EB, Spear FS, Shemella PT, Nayak SK, Lanzirrotti A (2010) TitaniQ under pressure: the effect of pressure and temperature on the solubility of Ti in quartz. *Contrib Mineral Petrol* 160:743–759
- Truckenbrodt J, Ziegenbein D, Johannes W (1997) Redox conditions in piston-cylinder apparatus: the different behavior of boron nitride and unfired pyrophyllite assemblies. *Am Mineral* 82:337–344
- Wark DA, Watson EB (2006) TitaniQ: a titanium-in-quartz geothermometer. *Contrib Mineral Petrol* 152:743–754
- Zinkernagel U (1978) Cathodoluminescence of quartz and its application to sandstone petrology. *Contrib Sediment Geol* 8:1–69